School of Pharmaceutical Sciences[1], Zhengzhou University; Key Laboratory of Targeting Therapy and Diagnosis of Critical Diseases[2]; Collaborative Innovation Center of New Drug Research and Safety Evaluation[3]; Henan Institute of Medical and Pharmaceutical Sciences[4], Zhengzhou University; BGI College[5], Zhengzhou University, Zhengzhou, Henan Province, China

Distribution of systemically administered nanoparticles during acute pancreatitis: effects of particle size and disease severity

Hong Qiang[1,2,3,#], Jianbo Li[4,#], Shuaishuai Wang[1,2,3], Tiange Feng[1,2,3], Huijie Cai[1,2,3], Zhilei Liu[4,5], Jingjing Yuan[1,2,3], Wanli Zhang[1,2,3], Jinjie Zhang[1,2,3,*], Zhenzhong Zhang[1,2,3,*]

Received November 2, 2021, accepted January 29, 2021

**Corresponding authors: Jinjie Zhang, Zhenzhong Zhang, School of Pharmaceutical Sciences, Zhengzhou University, No. 100 Kexue Road, Zhengzhou, Henan Province, China*
liger1029@126.com (J. Zhang), zhangzhenzhong@zzu.edu.cn (Z. Zhang)
[#]These authors contributed equally to this work.

Pharmazie 76: 180-188 (2021) *doi: 10.1691/ph.2021.0156*

Nanoparticles (NPs) promise to address current limitations for treating acute pancreatitis (AP) *via* inflammatory cell-mediated sequestration. However, very few studies have explored the influence of NP size on their behavior in different stages of AP. The present work investigated the biodistribution of IR780 loaded mesoporous silica nanoparticles (MSNs) with sizes of 60, 150 or 300 nm after intravenous administration to rats of mild AP (MAP) or severe AP (SAP). Four hours after administration, MSN_{150} was present to a much greater extent in the pancreas than MSN_{60} or MSN_{300}, irrespective of disease severity. MSN_{150} was present to a lower extent in pancreas, intestine and ascites in SAP than MAP rats, indicating weaker passive targeting in SAP rats. This may reflect greater blood loss and slower blood flow in SAP. These findings may guide the rational engineering of NPs with respect to particle size and disease severity for AP therapy.

1. Introduction

Acute pancreatitis (AP) is a common inflammatory disease of the pancreas, manifesting as abnormal pancreatic enzyme activation, inflammatory reactions, edema and necrosis of the pancreas (Boxhoorn et al. 2020). Inflammatory cells drive local and systemic immune responses, leading AP to progress in 10-20% of patients from mild acute pancreatitis (MAP) to severe disease (SAP) (Habtezion et al. 2019; Seppänen and Puolakkainen 2020). SAP is associated with severe systemic inflammatory responses, organ failure and a higher risk of mortality (Garg and Singh 2019; Komara et al. 2020). Currently, the primary treatments are supportive care and surgery (van Dijk et al. 2017; Hines and Pandol, 2019; Chaitoff et al. 2020). Effective treatments other than surgery are urgently needed.

Nanoparticles (NPs) have attracted considerable attention in recent years for treating various diseases (Paliwal et al. 2020; Zhen et al. 2019; Kim et al. 2018). To target damaged tissues after systemic administration, NPs should show efficient passive targeting (Kang et al. 2020; Alavi and Hamidi, 2019; Thao et al. 2016). NP size plays a crucial role in determining passive targeting efficacy (Nabeshi et al. 2010; Kang et al. 2020). For example, the size of tumor-targeting NPs should be optimized to exploit the enhanced permeability and retention (EPR) effect (Shi et al. 2020; Fang et al. 2020). Comparison of silica nanoconjugates (NCs) with sizes of 20, 50, or 200 nm showed that NCs of 50 nm penetrated MCF-7 human breast tumors and 4T1 metastatic lung tumors *in vivo* to the greatest extent and were cleared from the tumor most slowly (Tang et al. 2014).

Inflammation-related diseases often involve extravasation through leaky vasculature and subsequent inflammatory cell-mediated sequestration, a process known as ELVIS (Koziolová et al. 2018; Yuan et al. 2012). As AP is associated with dramatically increased vascular permeability (Tomkötter et al. 2016; Liu et al. 2015), the magnitude of ELVIS may change during progression from MAP to SAP. How the size of NPs affects their behavior in AP and therefore their therapeutic efficacy remains unclear. In addition, the possible alteration in ELVIS as AP progresses may influence passive targeting by NPs. Thus, studies are needed to establish the optimal NP size for treating AP in different stages.

Here, mesoporous silica nanoparticles (MSNs) with diameters of 60, 150 or 300 nm were prepared, loaded with the fluorescent dye IR780, and injected into rat models of MAP and SAP. MSNs were used as model nanoparticles because of their controllable particle size, non-invasiveness, biocompatibility and potential applications in AP therapy (Hua et al. 2015; Hoang Thi et al. 2019; Croissant et al. 2018). Our study may help guide the selection of optimal NPs according to AP severity.

2. Investigations, results and discussion

To investigate the desired size of NPs for AP therapy, we prepared MSNs of 60, 150 or 300 nm and investigated their biodistribution based on disease severity. Size of MSNs was controlled by varying the concentration of cetyltrimethylammonium bromide (CTAB) (Gan et al. 2012; Ma et al. 2018). As the CTAB concentration increased from 1.5 to 6.3 mM, MSN size grew from 60 to 300 nm (Table). Reaction temperature also strongly influenced MSN size. The same CTAB concentration led to MSN_{150} at 50 °C but MSN_{300} at 30 °C. MSNs of all three sizes possessed excellent monodisper-

Table: Amounts of reactants and reaction temperatures for synthesis of MSNs of different sizes

Sample	CTAB (g)	NH3·H2O (mL)	H2O (mL)	TEOS (mL)	Temp (°C)
MSN60	0.279	12	500	1.394	50
MSN150	0.279	12	220	1.394	50
MSN300	0.279	12	110	1.394	30

The subscript number indicates the approximate size of each sample in nm.
CTAB, cetyltrimethylammonium bromide; TEOS, tetraethyl orthosilicate

sity, uniformity and spherical shape, based on transmission electron microscopy (Fig. 1A). The hydrodynamic size was 75.4±4.6 nm for MSN_{60}, 170.3±6.0 nm for MSN_{150}, and 435.9±4.4 nm for MSN_{300}, as measured by dynamic light scattering (Fig. 1B). The hydrodynamic size of MSNs based on dynamic light scattering slightly exceeded that based on electron microscopy, mainly due to hydration of MSNs in solution (Smith et al. 2019). The difference may also reflect that dynamic light scattering yields an intensity weighted mean, while electron microscopy yields a number mean. MSNs of all three sizes showed a negative zeta potential of about -22.0 mV (Fig. 1C), eliminating surface charge as an explanation for any differences in biodistribution that we might observe.

X-ray diffraction (XRD) studies indicated that all the synthesized MSNs possessed partially ordered frameworks (Fig. 1D). Nitrogen adsorption-desorption isotherms indicated a Brunauer-Emmett-Teller surface area of 599.3 $m^2 g^{-1}$ for MSN_{60}, 577.4 $m^2 g^{-1}$ for MSN_{150} and 521.4 $m^2 g^{-1}$ for MSN_{300} (Fig. 1E). All MSN sizes exhibited typical type-IV isotherms, indicating the presence of cylindrical pores. All MSN sizes exhibited similar Barret-Joyner-Halenda pore size distributions (Fig. 1F), indicating a pore diameter of about 1.19 nm. The appearance of a hysteresis loop confirmed the cylindrical shape of pores (Ma et al. 2018; Mai et al. 2017).

The dye FITC has often been used to track MSN biodistribution (Tran and Lee 2018) but covalently conjugating the dye to MSNs requires complicated synthesis (Liu et al. 2018). In addition, FITC fluorescence often self-quenches when the dye interacts with proteins *in vivo*. Here we developed a new MSN labeling method using the near-infrared (NIR) red fluorescent probe IR780, a lipophilic cationic heptamethine dye. IR780 absorbs at 700-900 nm, where biological tissues are transparent, making it quite useful for *in vivo* applications (Alves et al. 2018; Li et al. 2017). The tertiary amine group on IR780 can interact with MSNs through electrostatic interaction, facilitating dye loading (Li et al. 2017). Indeed, IR780 was efficiently loaded into MSNs of all three sizes through simple mixing: encapsulation efficiencies were 67.31±5.10% for MSN_{60}, 65.33±4.58% for MSN_{150}, and 60.94±6.61% for MSN_{300}. The corresponding drug-loading coefficients were 18.39±2.16%, 17.97±3.51% and 16.69±2.08% (Fig. 2D).

Dynamic light scattering indicated average hydrodynamic diameters of 80.3±7.4 nm for MSN_{60}/IR780, 172.9±6.9 nm for MSN_{150}/IR780 and 439.1±6.3 nm for MSN_{300}/IR780 (Fig. 2B), indicating little change due to dye loading. Transmission electron microscopy confirmed this (Fig. 2A). The zeta potential of all three MSNs/IR780 was nearly neutral at about -2.0 mV (Fig. 2C), so we hypothesized that that much of the IR780 was adsorbed to the MSN surface via electrostatic attraction.

Stable encapsulation of drugs and fluorescent dyes in the circulation is important for reducing off-target effects and reducing background during bioimaging. Therefore, release of IR780 from MSNs/IR780 was evaluated *in vitro* using the dialysis method. During 48 h, cumulative leakage of IR780 was 5.49±1.20% from MSN_{60}/IR780, 7.27±0.58% from MSN_{150}/IR780 and 7.63±1.24% from MSN_{300}/IR780 (Fig. 2E). These results suggest the potential for MSNs of all three sizes to remain stable in circulation, with negligible drug leakage.

Amylase activity is considered a key indicator of the severity of pancreatic injury in AP (Kumaravel et al. 2015; Mandal et al. 2019). At 2 and 4 h after induction with sodium taurocholate, MAP and SAP rats showed markedly higher serum amylase activity than sham-operated animals (***$p < 0.001$, Fig. 3A). At 4 h, SAP animals showed significantly higher serum amylase activity than MAP animals (9840.78±1867.10 vs. 4845.45±1323.40 U/dl, ***$p < 0.001$), consistent with greater severity of pancreatitis. Ascites volume increases during AP progression due to plasma leakage from the circulation (Yan et al. 2004; Zhang et al. 2010), and we found that the ascites mass increased from 3.96±0.89 to 6.73±1.32 g in the MAP group and from 6.65±0.75 to 9.13±1.08 g in the SAP group by 4 h after disease induction (Fig. 3B). In contrast, no increase was observed in the sham group. Significantly less ascites was recovered from MAP animals than from SAP animals at 2 and 4 h after disease induction (**$p < 0.01$, ***$p < 0.001$), consistent with the difference in disease severity.

In AP, pro-inflammatory cytokines such as TNF-α and IL-6 are released from injured pancreatic acinar cells into the blood circulation (Pendharkar et al. 2018). Thus, levels of these cytokines are considered important indicators of AP progression (Soyalp et al. 2017). At 2 and 4 h after disease induction, SAP animals showed significantly higher TNF-α levels (*$p < 0.05$, **$p < 0.01$) and marginally higher IL-6 levels than MAP animals (Fig. 3C).

The degree of pancreatic injury in animals was assessed by histology, together with the degree of lung injury, which is the most frequent systemic complication in AP (Basios et al. 2016; Lin et al. 2016). At 4 h after disease induction, MAP and SAP animals showed disrupted arcinar architecture, vacuolization, inflammatory cell infiltration and necrosis of arcinar cells within the pancreas, whereas sham animals showed healthy histology (Fig. 3E). Pancreatic injury was more severe in SAP animals, which showed a large area of necrosis and hemorrhage within the pancreas parenchyma, in contrast to the minimal inflammatory cell infiltration and slight parenchyma necrosis in MAP animals. Similarly, lungs in SAP animals showed alveolar wall thickening and collapse, whereas minimum histological change was observed in MAP animals. Consistent with these histology findings, pancreas and lung sections showed higher TNF-α and IL-6 levels in disease animals than in sham controls, with the highest levels in SAP animals (Fig. 3E).

These results confirm that we were able to create MAP and SAP models in rats. They also suggest that ELVIS is weaker in more severe disease, justifying our investigation of MSN biodistribution in different stages of AP.

Rats were intravenously injected with MSNs/IR780 of different sizes, and major organs were collected at 2 and 4 h later and their fluorescence was measured. At 2 h after injection into MAP animals, MSNs of all sizes distributed mainly to the liver, lung and spleen, followed by subcutaneous fat, pancreas and duodenum (Fig. 4A). Scarce fluorescence signal was observed in heart, kidney and brain. By 4 h after injection, fluorescence signal had increased in pancreas, intestine and ascites (Fig. 4B), indicating gradual MSN leakage from blood circulation into pancreas and ascites. We suppose that the leakage was due to ELVIS.

The distribution of MSNs of all sizes in SAP rats was similar to that in MAP animals 2 h after injection (Fig. 4C). Four hours after injection, however, the fluorescence signal in all tissues and ascites was weaker in SAP animals than in MAP animals, despite the fact that SAP animals produced much more ascites (Fig. 3B). This may reflect weakening ELVIS with more severe disease, which reduces MSN passive targeting.

In MAP rats, MSN_{150}/IR780 was present in pancreas at higher levels than MSN_{60}/IR780 or MSN_{300}/IR780 at 2 and 4 h after injection, indicating excellent accumulation in the pancreas (Fig. 4 E). In contrast, at both time points, MSN_{150}/IR780 was present to a greater extent than the other MSNs in intestine and ascites (Fig. 4A-B). This may indicate potential for MSNs of this size to target intestinal leakage in AP. Such leakage allows bacteria and endotoxins to enter the blood and lymph, where they can cause infection and inflammation (Barbeiro et al. 2016; Lu et al. 2017).

In contrast to their behavior in MAP animals, MSN_{60}/IR780 in SAP rats accumulated in the pancreas to a significantly greater extent than the other MSNs by 2 h after injection (*$p < 0.05$, ***$p < 0.001$, Fig. 4 F). This difference was probably due to the more rapid accumulation of MSN_{60}/IR780 than MSN_{150}/IR780 in pancreas, since by 4 h after injection, MSN_{150}/IR780 had accumulated in pancreas to a markedly greater degree than MSN_{60}/IR780 or MSN_{300}/IR780 (**$p < 0.01$, ***$p < 0.001$, Fig. 4 F). As in MAP animals, MSN_{150}/IR780 in SAP rats was present in ascites to a greater extent than the other MSNs. MSN_{150}/IR780 showed the highest fluorescence signal in intestine and ascites among all MSNs (Fig. 4A-B). Nevertheless, MSN_{150}/IR780 showed a significantly lower fluorescence signal in pancreas, intestine and ascites in SAP rats than in MAP animals, consistent with decreased passive targeting ability as a

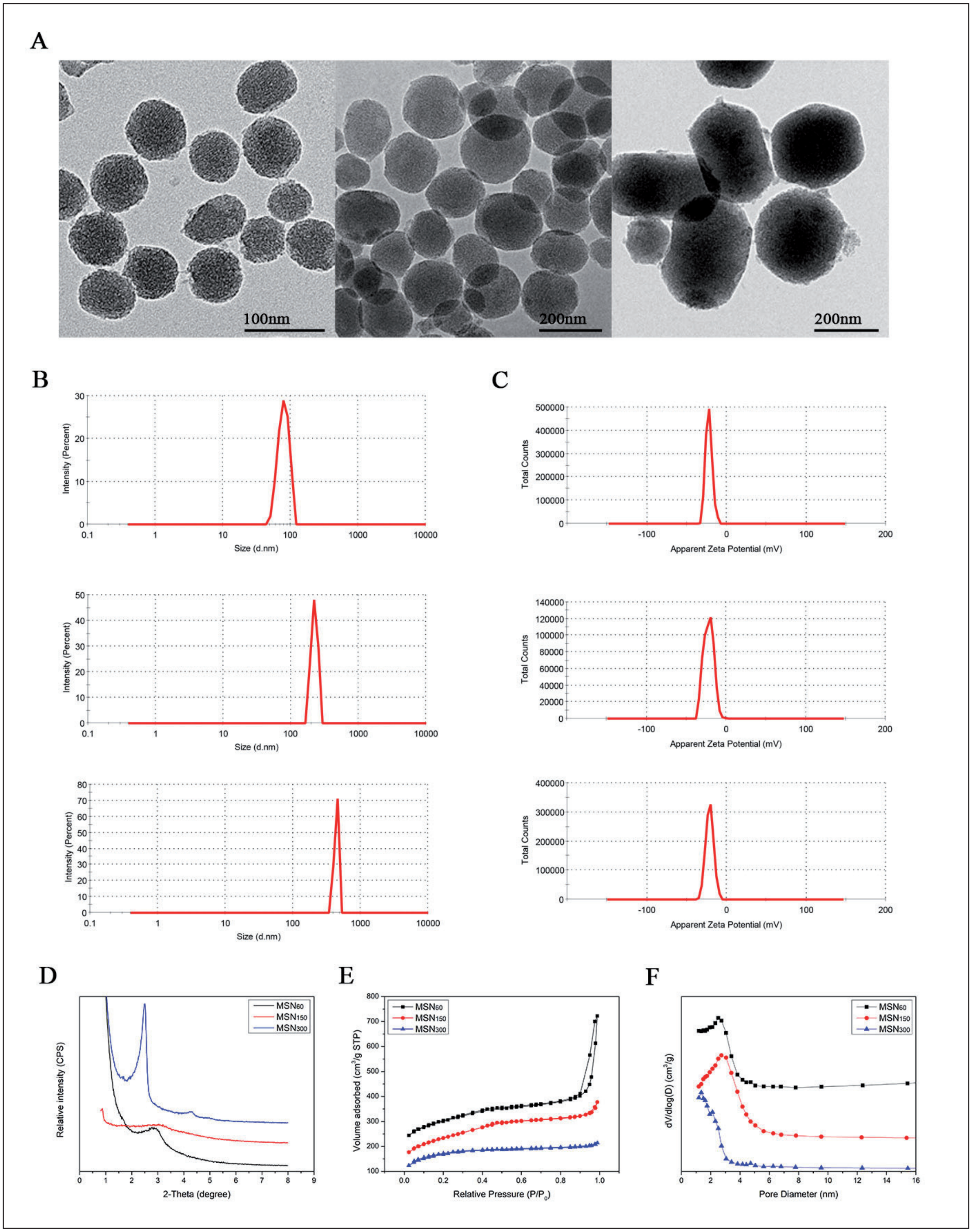

Fig. 1: Characterization of MSNs. Representative results for triplicate experiments are shown. (A) Transmission electron micrographs of MSNs with diameters of 60, 150 or 300 nm. (B) Size distribution of MSNs, as measured by dynamic light scattering. (C) Zeta potential of MSNs. (D) Powder X-ray diffraction patterns of MSNs. (E) Nitrogen adsorption-desorption isotherms of MSNs. (F) Pore size distribution curves of MSNs.

result of more severe pancreatitis. MSN_{300}/IR780 showed the weakest retention in tissues at 2 and 4 h after injection.

Our study suggests that the biodistribution of MSNs against AP depends on NP size as well as disease severity. MSN_{150} accumulated in the pancreas and ascites of a rat model of AP to a much greater extent than MSN_{60} or MSN_{300}. Moreover, progression from MAP to SAP was associated with greater accumulation of MSNs in ascites and loss of MSNs from pancreas because

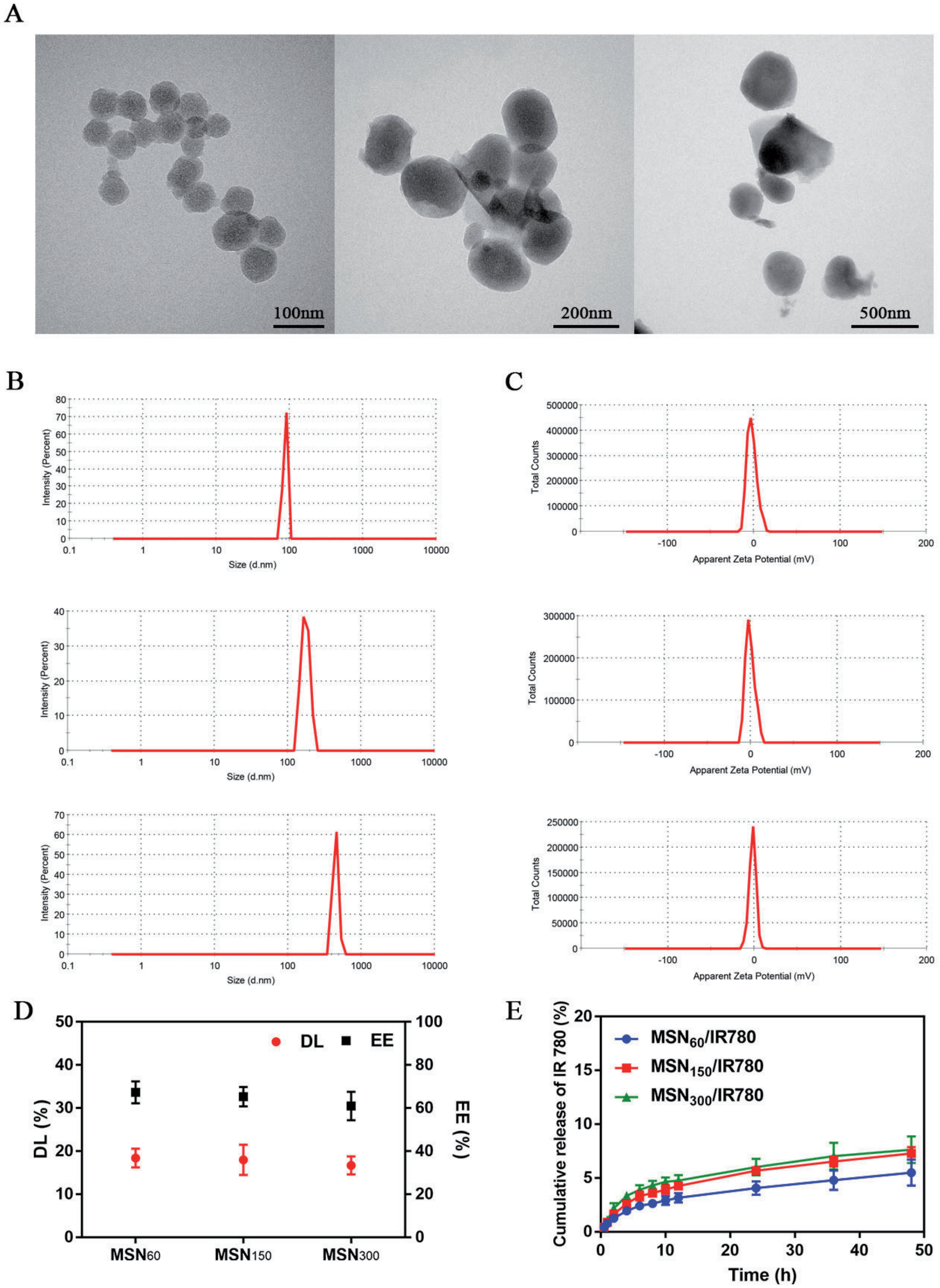

Fig. 2: Characterization of IR780-loaded MSNs with diameters of 60, 150 or 300 nm. Representative results are shown from triplicate experiments. (A) Representative transmission electron micrographs. (B) Size distribution. (C) Zeta potential. (D) Drug-loading coefficient (DL) and encapsulation efficiency (EE). (E) Release of IR780 from MSNs/IR780 *in vitro*. Data in panels D-E are mean±SD (n=3).

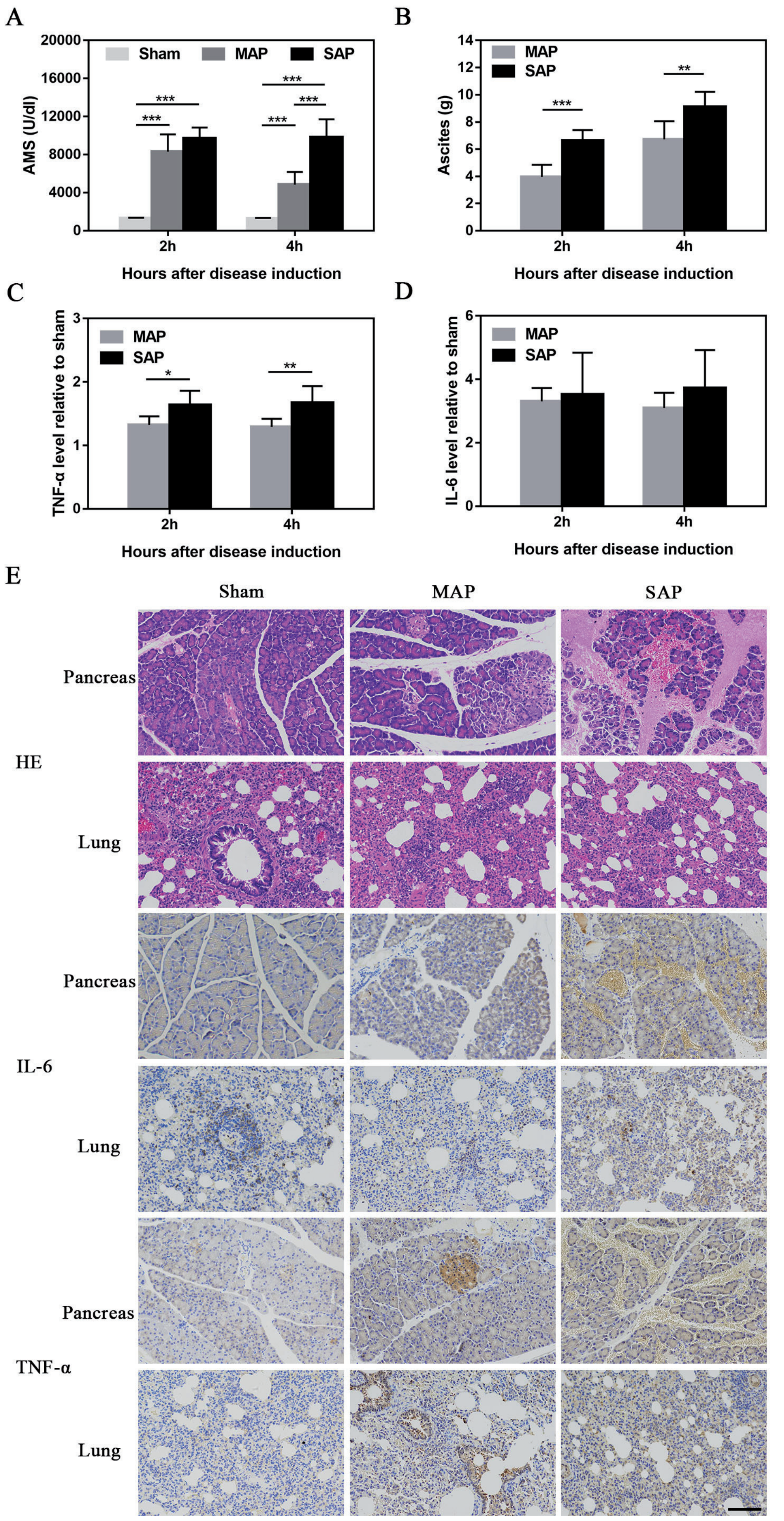

Fig. 3: Evaluation of rat models of mild acute pancreatitis (MAP) and severe acute pancreatitis (SAP). (A) Amylase activity in serum (AMS). (B) Mass of ascites collected. (C-D) Relative TNF-α and IL-6 levels, expressed as fold increase above levels in sham animals. (E) Representative histology and immunohistochemistry of pancreas and lung tissue from disease or sham animals. Scale bar = 100 µm. Data in panels A-D are mean±SD (n = 8). *$p < 0.05$, **$p < 0.01$, ***$p < 0.001$.

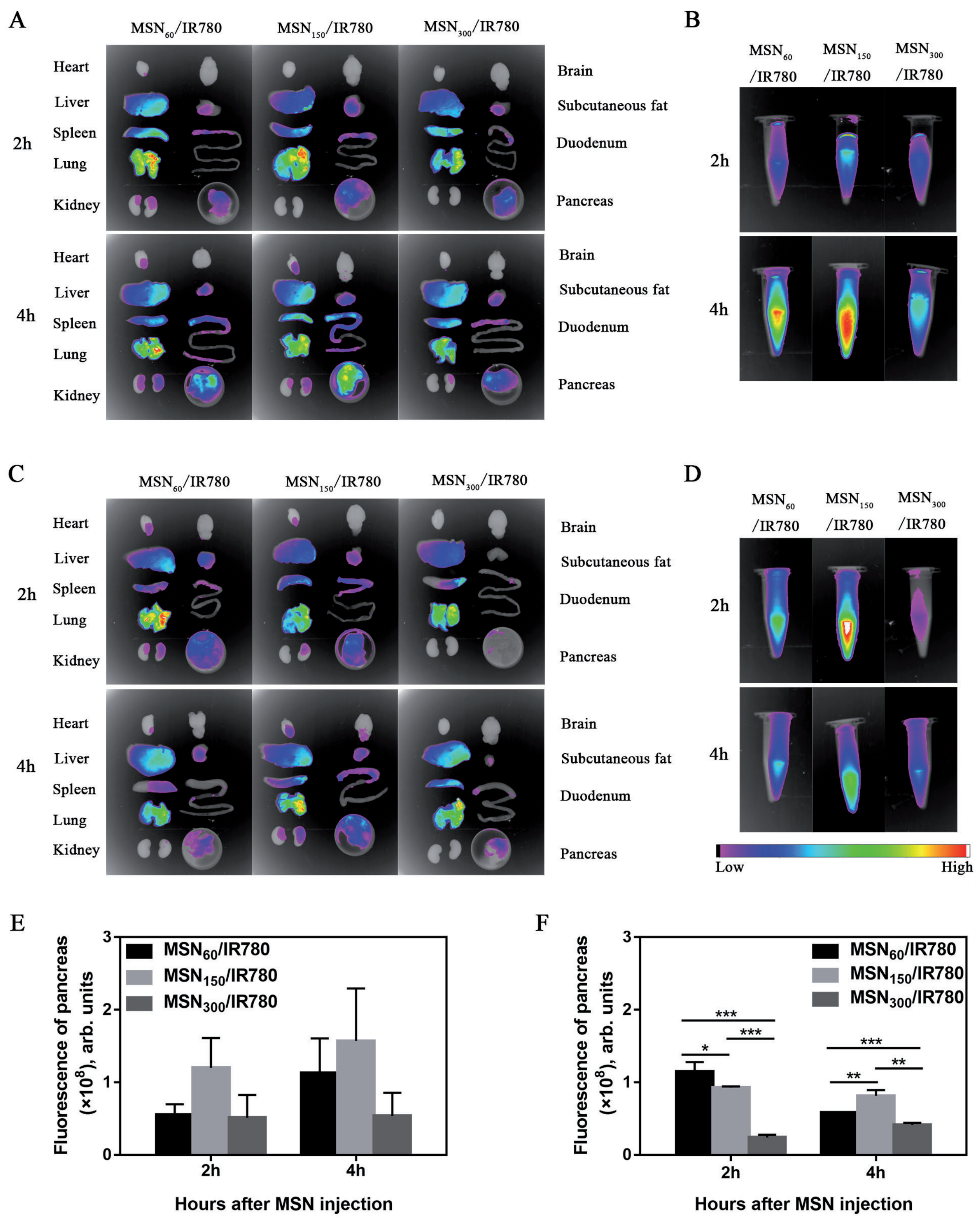

Fig. 4: Biodistribution of MSNs/IR780 in rat models of mild acute pancreatitis (MAP) and severe acute pancreatitis (SAP). (A, C) Representative *ex vivo* fluorescence imaging of major organs and tissues from (A) MAP or (C) SAP animals at 2 h and 4 h after injection. (B, D) Representative fluorescence imaging of ascites collected from (B) MAP and (D) SAP rats. (E-F) Semiquantitative analysis of fluorescence intensity of the pancreas in (E) MAP and (F) SAP rats. Data in panels E-F are mean ± SD (n=8). $*p < 0.05$, $**p < 0.01$, $***p < 0.001$.

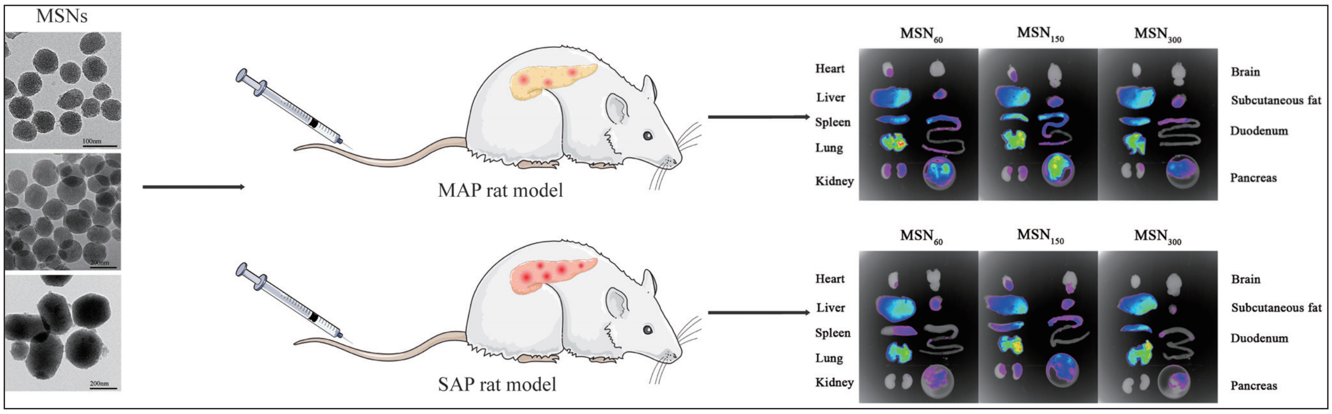

Fig. 5: Graphical overview about study design and results.

of greater fluid loss. This study underscores the significance of evaluating NP biodistribution during AP progression, because the distribution depends on particle size and disease severity. These results provide guidance for selecting appropriate NPs according to AP severity.

3. Experimental

3.1. Materials

IR780 iodide was provided by Sigma–Aldrich (St. Louis, MO, USA). Cetyltrimethylammonium bromide (CTAB) and tetraethyl orthosilicate (TEOS) were purchased from Aladdin Reagent Co., Ltd (Shanghai, China). Sodium taurocholate was obtained from Aobox Biotechnology (Beijing, China). All other chemicals and reagents were of analytical grade. Serum amylase assay kits were provided by Nanjing Jiancheng Bioengineering Institute (Nanjing, China). IL-6 and TNF-α ELISA kits were purchased from Dakewe Biotech Co., Ltd (Shenzhen, China).

3.2. Animals

Male Wistar rats (180–220 g) were supplied by the Laboratory Animal Center, Zhengzhou University. All animal experiments were conducted with approval from the Life Science Research Ethics Committee of Zhengzhou University. All applicable international, national, and/or institutional guidelines for the care and use of animals were followed. Rats were acclimatized before experiments and provided free access to food and water.

3.3. Synthesis of MSNs

MSNs were synthesized in three sizes using the base-catalyzed sol–gel method (Gan et al. 2012; He et al. 2011). MSNs with mean particle sizes of 60 nm (MSN$_{60}$), 150 nm (MSN$_{150}$) or 300 nm (MSN$_{300}$) were prepared by altering the amounts of reactants and reaction temperature (Table 1). CTAB (0.279 g) was dissolved in distilled water at 30 °C or 50 °C already containing 12 mL ammonium hydroxide (29 wt%). Under vigorous stirring, 1.39 mL TEOS was added to the mixture. After 2 h, the reaction mixture was centrifuged (12,544 *g*) for 10 min. The solid residue was washed with distilled water and ethanol, followed by vacuum drying. The CTAB-templates were removed by reflux extraction in a mixture of 100 mL ethanol and 1 mL hydrochloric acid (36–38%) for 6 h at 80 °C. After centrifugation, MSNs were collected, washed with ethanol and distilled water. Finally, the obtained MSNs were dried under vacuum at low temperature.

3.4. Preparation of IR780-loaded MSNs (MSNs/IR780)

MSNs were loaded with the NIR fluorescent dye IR780 according to a previous report (Yang et al. 2019) but with minor modifications. First, 12 mg MSNs and 4 mg IR780 were added to 1 mL methanol, and the mixture was protected from light at room temperature and stirred for 24 h. Then MSNs/IR780 were collected after centrifugation, washed with 10% (v/v) methanol/water to remove free IR780, centrifuged again and dried under vacuum.

To analyze the amount of IR780 incorporated into MSNs, 2 mg MSNs/IR780 were washed with methanol and centrifuged repeatedly until the supernatant became colorless. The supernatants were pooled, and absorbance at 780 nm was monitored by a UV-vis spectrophotometer. The encapsulation efficiency (EE) and drug-loading coefficient (DL) were calculated using the following equations:

$$\mathrm{EE\%} = \frac{\text{weight of IR780 incorporeted into MSNs}}{\text{weight of IR780 initially added}} \times 100\%$$

$$\mathrm{DL\%} = \frac{\text{weight of IR780 incorporeted into MSNs}}{\text{weight of IR780-loaded MSNs}} \times 100\%$$

3.5. Characterization of MSNs

The morphology of the resulting MSNs was examined using a transmission electron microscope (TEM; JEM-2100F, Japan). TEM specimens were prepared by placing the MSN suspension onto copper grids. Average particle size, size distribution and zeta potential of MSNs diluted by distilled water (1:10) were measured in triplicate using a Malvern ZS90 (Malvern, Worcestershire, UK). X-ray diffraction patterns were recorded using an X'Pert PRO MPD (PANalytical, Almelo, Netherlands). X-ray diffractograms were obtained from 0° to 10° at intervals of 0.2° with a count time of 0.4 s. The MSN surface was analyzed based on nitrogen adsorption-desorption isotherms using a NOVA Touch apparatus (Quantachrome Instruments, Boynton Beach, FL, USA). Each experiment was conducted in triplicate.

3.6. In vitro drug release studies

In vitro release profiles of IR780 from MSNs were determined using dynamic dialysis (Si et al. 2020). In brief, 2 mL of MSNs/IR780 were placed in dialysis bags (molecular weight cut-off, 8-14 kDa; Viskase, Darien, IL, USA). These bags were immersed in 20 mL phosphate-buffered saline (PBS, pH 7.4) with 0.5% Tween 80, and incubated at 37 °C under gentle shaking at 100 rpm. At specified time points, 1 ml of the release media was aspirated and supplemented with 1 ml of fresh media. Concentration of IR780 in the sample was determined based on absorbance at 780 nm using a UV-vis spectrometer. Each experiment was conducted in triplicate.

3.7. Rat models of MAP and SAP

Rat models were generated using sodium taurocholate injection as described (Li et al. 2015; Wang et al. 2018) with slight modifications. Briefly, male Sprague-Dawley rats (250-300 g) were fasted overnight before surgery and then divided into three groups (n=8 in each group). After inducing anesthesia with 1% pentobarbital sodium (45 mg/kg), the abdomen cavity of the rat was exposed and the bile-pancreatic duct was cannulated with a 27-gauge needle. The MAP model was generated by infusing sterile 1% sodium taurocholate (10 mg/kg) in a retrograde fashion into the distal end of the bile-pancreatic duct at a flow rate of 0.1 mL/min. The distal end was ligated to block backflow of taurocholate into the duodenum. The SAP model was established in the same way, except that 5% sodium taurocholate (50 mg/kg) was used. After infusion, the needle and ligature were removed, and the abdominal wound was immediately sutured. All the experimental operations were carried out under sterile conditions. Sham-operated animals underwent the abdominal operation, and the pancreas was simply turned over several times before closure.

At 2 and 4 h after surgery, rats were anesthetized and subjected to laparotomy, when an absorbent ball was placed into the abdomen for 3 min to collect ascites. Next left ventricular blood was sampled for assay of TNF-α, IL-6 and amylase (see section 3.8). Finally, rats were sacrificed, and pancreas and lungs were immediately dissected out for histological examination and immunohistochemistry (see section 3.9).

3.8. Serum assays

After centrifugation of the blood samples (500 *g*, 15 min), the serum was obtained and stored at −80 °C until analysis for the pro-inflammatory cytokines TNF-α and IL-6 using commercial ELISA kits following the manufacturer's procedure.

3.9. Histology and immunohistochemistry

Immediately after harvesting, pancreas and lungs were fixed in 4% formaldehyde for at least 48 h at 4 °C. Then the tissue was embedded in paraffin, cut at a thickness of

5 µm, stained with hematoxylin and eosin, and observed under an optical microscope. Severity of pancreatitis was assessed based on edema, inflammatory cell infiltration, vacuolization, vascular congestion, alveolar wall thickening and collapse, destruction of the alveolar wall, and necrosis (Boxhoorn et al. 2020; Weis et al. 2019). Alternatively, fixed sections were immunostained against TNF-α and IL-6 in pancreas and lungs (Li et al. 2015). These tissue sections were sequentially subjected to antigen retrieval, blocking endogenous peroxidase activity and serum sealing. Next, NF-α and IL-6 expression were detected using rabbit anti-rat antibodies (diluted 1:500) and the Streptavidin Biotin Complex Detection kit (Boster, Wuhan, China). All sections were counterstained with hematoxylin stain solution for about 3 min to label nuclei. After dehydration and mounting, these sections were examined by optical microscopy (Zeiss Axiovert 40).

3.10. Biodistribution of MSNs in MAP and SAP rats

MAP and SAP rats were randomly allocated to receive MSN_{60}/IR780, MSN_{150}/IR780 or MSN_{300}/IR780 (eight animals per group) via intravenous injection (2 mg/kg in IR780). Two and four hours after injection, rats were sacrificed and ascites were collected into tubes. The following tissues were immediately dissected out: pancreas, kidney, heart, lung, liver, spleen, brain, subcutaneous fat and duodenum. These tissues were examined using an F PRO® *in vivo* imaging system (Bruker, Billerica, MA, USA).

3.11. Statistical analysis

Differences between two groups were assessed for significance using Student's t test, while differences among more than two groups were assessed using one-way ANOVA, followed by Tukey's test. Significant differences were indicated by $^{*}p < 0.05$, $^{**}p < 0.01$, and $^{***}p < 0.001$.

Acknowledgments: Our study was supported by the National Natural Science Foundation of China (81703433 and 81703422), China Postdoctoral Science Foundation (2017M622381), Key Scientific and Technological Project of Henan Province (202102310160) and the Project of the Basic Research Fund of the Henan Institute of Medical and Pharmacological Sciences (yyyjk201801).

Conflicts of interest: None declared

References

Alavi M, Hamidi M (2019) Passive and active targeting in cancer therapy by liposomes and lipid nanoparticles. Drug Metab Pers Ther 34: doi: 10.1515/dmpt-2018-0032.

Alves C, Lima-Sousa R, De Melo-Diogo D, Louro R, Correia I (2018) IR780 based nanomaterials for cancer imaging and photothermal, photodynamic and combinatorial therapies. Int J Pharm 542: 164–175.

Barbeiro D, Koike M, Coelho A, Da Silva F, Machado M (2016) Intestinal barrier dysfunction and increased COX-2 gene expression in the gut of elderly rats with acute pancreatitis. Pancreatology 16: 52–56.

Basios N, Lampropoulos P, Papalois A, Lambropoulou M, Pitiakoudis M, Kotini A, Simopoulos C, Tsaroucha A (2016) Apigenin attenuates inflammation in experimentally induced acute pancreatitis-associated lung injury. J Invest Surg 29: 121–127.

Boxhoorn L, Voermans R, Bouwense S, Bruno M, Verdonk R, Boermeester M, Van Santvoort H, Besselink M (2020) Acute pancreatitis. Lancet 396: 726–734.

Chaitoff A, Cifu A, Niforatos J (2020) Initial management of acute pancreatitis. JAMA 323: 2331–2332.

Croissant J, Fatieiev Y, Almalik A, Khashab N (2018) Mesoporous silica and organosilica nanoparticles: physical chemistry, biosafety, delivery strategies, and biomedical applications. Adv Healthc Mater 7: doi: 10.1002/adhm.201700831.

Fang J, Islam W, Maeda H (2020) Exploiting the dynamics of the EPR effect and strategies to improve the therapeutic effects of nanomedicines by using EPR effect enhancers. Adv Drug Deliv Rev 157: 142–160.

Gan Q, Dai D, Yuan Y, Qian J, Sha S, Shi J, Liu C (2012) Effect of size on the cellular endocytosis and controlled release of mesoporous silica nanoparticles for intracellular delivery. Biomed Microdevices 14: 259–270.

Garg P, Singh V (2019) Organ failure due to systemic injury in acute pancreatitis. Gastroenterology 156: 2008–2023.

Habtezion A, Gukovskaya A, Pandol S (2019) Acute pancreatitis: a multifaceted set of organelle and cellular interactions. Gastroenterology 156: 1941–1950.

He Q, Zhang Z, Gao F, Li Y, Shi J (2011) In vivo biodistribution and urinary excretion of mesoporous silica nanoparticles: effects of particle size and PEGylation. Small 7: 271–280.

Hines O, Pandol S (2019) Management of severe acute pancreatitis. BMJ (Clinical research ed.), 367: l6227.

Hoang Thi T, Cao V, Nguyen T, Hoang D, Ngo V, Nguyen D (2019) Functionalized mesoporous silica nanoparticles and biomedical applications. Materials science, engineering. C, Materials for Biological Applications 99: 631–656.

Hua K, Sheng X, Li TT, Wang LN, Zhang YH, Huang ZJ, Ji H (2015) The edaravone and 3-n-butylphthalide ring-opening derivative 10b effectively attenuates cerebral ischemia injury in rats. Acta Pharmacol Sin 36: 917–927.

Kang H, Rho S, Stiles W, Hu S, Baek Y, Hwang D, Kashiwagi S, Kim M, Choi H (2020a) Size-dependent EPR effect of polymeric nanoparticles on tumor targeting. Adv Healthc Mater 9: e1901223.

Kim D, Shin K, Kwon S, Hyeon T (2018) Synthesis and Biomedical Applications of Multifunctional Nanoparticles. Advanced materials (Deerfield Beach, Fla.), 30: e1802309.

Komara N, Paragomi P, Greer P, Wilson A, Breze C, Papachristou G, Whitcomb D (2020) Severe acute pancreatitis: capillary permeability model linking systemic inflammation to multiorgan failure. Am J Physiol Gastrointest Liber Physiol 319: G573–G83.

Koziolová E, Venclíková K, Etrych T (2018) Polymer-drug conjugates in inflammation treatment. Physiol Res 67: S281–S292.

Kumaravel A, Stevens T, Papachristou GI, Muddana V, Bhatt A, Lee PJ, Holmes J, Lopez R, Whitcomb DC, Parsi MA (2015) A model to predict the severity of acute pancreatitis based on serum level of amylase and body mass index. Clin Gastroenterol Hepatol 13: 1496-1501.

Li J, Zhang J, Fu Y, Sun X, Gong T, Jiang J, Zhang Z (2015) Dual pancreas- and lung-targeting therapy for local and systemic complications of acute pancreatitis mediated by a phenolic propanediamine moiety. J Control Release 212: 19–29.

Li S, Johnson J, Peck A, Xie Q (2017) Near infrared fluorescent imaging of brain tumor with IR780 dye incorporated phospholipid nanoparticles. J Translat Med 15: 18.

Lin Z, Ku C, Guan Y, Xiao H, Shi X, Wang H, Bian Z, Tsang S, Zhang H (2016) Dihydro-resveratrol ameliorates lung injury in rats with cerulein-induced acute pancreatitis. Phytother Res 30: 663–670.

Liu L, Li Y, Fan L, Zhao Q, Wang D, Cheng S, Zhang A, Qin Y, Zhang B (2015) Effect of vascular bradykinin on pancreatic microcirculation and hemorheology in rats with severe acute pancreatitis. Eur Rev Med Pharmacol Sci 19: 2646–2650.

Liu XN, Kang JJ, Wang H, Huang T, Li C (2018) Construction of fluorescein isothiocyanate-labeled MSNs/PEG/lycorine/antibody as drug carrier for targeting prostate cancer cells. J Nanosci Nanotechnol 18: 4471–4477.

Lu F, Wang F, Chen Z, Huang H (2017) Effect of mesenchymal stem cells on small intestinal injury in a rat model of acute necrotizing pancreatitis. Stem Cell Rse Ther 8: 12.

Ma B, He L, You Y, Mo J, Chen T (2018) Controlled synthesis and size effects of multifunctional mesoporous silica nanosystem for precise cancer therapy. Drug Deliv 25: 293–306.

Mai Z, Chen J, Hu Y, Liu F, Fu B, Zhang H, Dong X, Huang W, Zhou W (2017) Novel functional mesoporous silica nanoparticles loaded with Vitamin E acetate as smart platforms for pH responsive delivery with high bioactivity. J Coll Interface Sci 508: 184–195.

Mandal N, Bhattacharjee M, Chattopadhyay A, Bandyopadhyay D (2019) Point-of-care-testing of α-amylase activity in human blood serum. Biosens Bioelectron 124-125: 75-81.

Nabeshi H, Yoshikawa T, Matsuyama K, Nakazato Y, Arimori A, Isobe M, Tochigi S, Kondoh S, Hirai T, Akase T, Yamashita T, Yamashita K, Yoshida T, Nagano K, Abe Y, Yoshioka Y, Kamada H, Imazawa T, Itoh N, Tsunoda S, Tsutsumi Y (2010) Size-dependent cytotoxic effects of amorphous silica nanoparticles on Langerhans cells. Pharmazie 65: 199–201.

Paliwal R, Paliwal S, Kenwat R, Kurmi B, Sahu M (2020) Solid lipid nanoparticles: a review on recent perspectives and patents. Expert Opin Ther Patents 30: 179–194.

Pendharkar S, Singh R, Chand S, Cervantes A, Petrov M (2018) Pro-inflammatory cytokines after an episode of acute pancreatitis: associations with fasting gut hormone profile. Inflammation Res 67: 339–350.

Seppänen H, Puolakkainen P (2020) Classification, severity assessment, and prevention of recurrences in acute pancreatitis. Scand J Surg 109: 53–58.

Shi Y, Van Der Meel R, Chen X, Lammers T (2020) The EPR effect and beyond: Strategies to improve tumor targeting and cancer nanomedicine treatment efficacy. Theranostics 10: 7921–7924.

Si W, Gao Y, Mei X, Wu C, Li J, Zhang J (2020) Mesoporous silica nanoparticles loaded with capsaicin and their oxidation resistance in meat preservation. Food Chem:128737.

Smith T, Kahiel Z, Leblond N, Ghorbani P, Farah E, Al-Awosi R, Cote M, Gadde S, Fullerton M (2019) Characterization of redox-responsive LXR-activating nanoparticle formulations in primary mouse macrophages. Molecules 24: 3751.

Soyalp M, Yalcin M, Oter V, Ozgonul A (2017) Investigation of procalcitonin, IL-6, oxidative stress index (OSI) plasma and tissue levels in experimental mild and severe pancreatitis in rats. Bratisl Lek Listy 118: 137–141.

Tang L, Yang XJ, Yin Q, Cai KM, Wang H, Chaudhury I, Yao C, Zhou Q, Kwon M, Hartman JA, Dobrucki IT, Dobrucki LW, Borst LB, Lezmig S, Helferich WG, Ferguson AL, Fan TM, Cheng JJ (2014) Investigating the optimal size of anticancer nanomedicine. Proc Natl Acad Sci USA, 111: 15344–15349.

Thao LQ, Byeon HJ, Lee C, Lee S, Lee ES, Choi HG, Park ES, Youn YS (2016) Pharmaceutical potential of tacrolimus-loaded albumin nanoparticles having targetability to rheumatoid arthritis tissues. Int J Pharm 497: 268–276.

Tomkötter L, Erbes J, Trepte C, Hinsch A, Dupree A, Bockhorn M, Mann O, Izbicki J, Bachmann K (2016) The effects of pancreatic microcirculatory disturbances on histopathologic tissue damage and the outcome in severe acute pancreatitis. Pancreas 45: 248–253.

Tran VA, Lee SW (2018) A prominent anchoring effect on the kinetic control of drug release from mesoporous silica nanoparticles (MSNs) J Colloid Interface Sci 510: 345–356.

Van Dijk SM, Hallensleben NDL, Van Santvoort HC, Fockens P, Van Goor H, Bruno MJ, Besselink MG, Grp DPS (2017) Acute pancreatitis: recent advances through randomised trials. Gut 66: 2024–2032.

Wang X, Chu L, Liu C, Wei R, Xue X, Xu Y, Wu M, Miao Q (2018) Therapeutic effects of Saussurea involucrata injection against severe acute pancreatitis- induced brain injury in rats. Biomed Pharmacother 100: 564–574.

Weis S, Heindl M, Carvalho T, Jentho E, Lorenz J, Sommerer I, Mössner J, Hoffmeister A (2019) Azithromycin does not improve disease severity in acute experimental pancreatitis. PloS one, 14: e0216614.

Yan W, Zhou Z, Chen Y, Gao H (2004) Role of COX-2 in microcirculatory disturbance in experimental pancreatitis. World J Gastroenterol 10: 2095–2098.

Yang Z, Wang J, Ai S, Sun J, Mai X, Guan W (2019) Self-generating oxygen enhanced mitochondrion-targeted photodynamic therapy for tumor treatment with hypoxia scavenging. Theranostics 9: 6809–6823.

Yuan F, Quan L, Cui L, Goldring S, Wang D (2012) Development of macromolecular prodrug for rheumatoid arthritis. Adv Drug Deliv Rev 64: 1205–1219.

Zhang J, Sio S, Moochhala S, Bhatia M (2010) Role of hydrogen sulfide in severe burn injury-induced inflammation in mice. Mol Med 16: 417–424.

Zhen X, Cheng P, Pu K (2019) Recent advances in cell membrane-camouflaged nanoparticles for cancer phototherapy. Small 15: e1804105.